

Non-invasive quantitative imaging of selective microstructure-sizes with magnetic resonance

Milena Capiglionj,^{1,2,3} Analía Zwick,^{1,4,*} Pablo Jiménez,^{1,2} and Gonzalo A. Álvarez^{1,2,4,†}

¹*Centro Atómico Bariloche, CONICET, CNEA, S. C. de Bariloche, 8400, Argentina*

²*Instituto Balseiro, CNEA, Universidad Nacional de Cuyo, S. C. de Bariloche, 8400, Argentina*

³*Support Center for Advanced Neuroimaging (SCAN),*

Institute of Diagnostic and Interventional Neuroradiology, University of Bern, Bern, 3010, Switzerland

⁴*Departamento de Física Médica, Instituto de Nanociencia y Nanotecnología, CNEA, CONICET, S. C. de Bariloche, 8400, Argentina*

Extracting reliable and quantitative microstructure information of living tissue by non-invasive imaging is an outstanding challenge for understanding disease mechanisms and allowing early stage diagnosis of pathologies. Magnetic Resonance Imaging is the favorite technique to pursue this goal, but still provides resolution of sizes much larger than the relevant microstructure details on in-vivo studies. Monitoring molecular diffusion within tissues, is a promising mechanism to overcome the resolution limits. However, obtaining detailed microstructure information requires the acquisition of tens of images imposing long measurement times and results to be impractical for in-vivo studies. As a step towards solving this outstanding problem, we here report on a method that only requires two measurements and its proof-of-principle experiments to produce images of selective microstructure sizes by suitable dynamical control of nuclear spins with magnetic field gradients. We design microstructure-size filters with spin-echo sequences that exploit magnetization “decay-shifts” rather than the commonly used decay-rates. The outcomes of this approach are quantitative images that can be performed with current technologies, and advance towards unravelling a wealth of diagnostic information based on microstructure parameters that define the composition of biological tissues.

The development of nanosized sensors with novel quantum technologies is aiming at nanoscale imaging of biological tissues for unveiling the biophysics of pathologies at such relevant scales [1–4]. Such imaging proposals are still based on invasive techniques. By contrast, Magnetic Resonance Imaging (MRI) has proven to be an excellent tool for acquiring non-invasive images, being applied on a daily basis for clinical diagnosis. However, the weak sensitivity for detecting the nuclear spins inherent to the biological tissues, typically limits the spatial resolution of in-vivo MRI to hundred of micrometers in pre-clinical scanners and to millimeters in clinical systems. This limitation imposes a challenge for existing methods to early detect diseases that produce changes at the cellular level [5–9]. Detecting these kind of pathologies in a development stage based on quantitative imaging of tissue microstructure parameters, will allow MRI to advance towards a new early diagnostic paradigm [7–13].

Diffusion Weighted MRI (DWI) is a promising tool to probe microstructure information based on monitoring the dephasing of the nuclear spin precession due to Brownian molecular motion [10, 14, 15]. The diffusion dynamics of molecules depends on tissue properties such as cell sizes, density, and other morphological features. A strong magnetic field gradient is applied to sense the microscopic motion of spins so that the precession frequency depends on their instantaneous position. In addition, modulating the gradient strength as a function of time allows to probe the time dependent diffusion process of the molecules within tissues [15–18]. These dynamical control techniques are based on the Hahn spin-echo concept [19] and its generalization to multiple echoes [20]. Within DWI they are called modulated gradient spin-echo (MGSE) sequences, where the phase ac-

cumulated by the spin’s precession is refocused at given times allowing to infer microscopic parameters in tissues and porous media [16, 18, 21–23]. However, obtaining detailed microstructure information is still challenging on in-vivo studies, as it requires tens of images demanding about an hour of acquisition time [11, 13, 23–26].

The decay of the nuclear spin signal under MGSE sequences is typically characterized by a decay-rate [14, 15]. Here, we report that these decaying signals manifest a “decay-shift” that can be exploited to selectively probe microstructure-sizes. We develop size-filters based on the Non-uniform Oscillating Gradient Spin-Echo (NOGSE) concept that contrast the signal generated by two spin-echo sequences [17, 18]. The method probes different diffusion time scales while factoring out other relaxation mechanisms induced by gradient-modulation imperfections and T_2 effects. We exploit the NOGSE modulations to selectively probe the spin-echo decay-shift for producing quantitative images based on contrast intensities that reflect the probability of finding a specific microstructure-size. The present approach requires only two measurements, therefore significantly reducing the acquisition time compared to state-of-the-art methods that typically require tens of measurements to obtain quantitative information on microstructure-sizes based on fitting parameters [11, 13, 23–27]. We analytically and experimentally demonstrate that these microstructure-size filters can be implemented with current technologies presenting a novel mechanism for quantitative and precision imaging diagnostic tools.

MRI of molecular-diffusion. The nuclear spins $S = \frac{1}{2}$ in molecules intrinsic to biological tissues, mainly from water’s protons, are typically observed on in-vivo MRI. They

interact with an external uniform magnetic-field $B_0\hat{z}$ and a magnetic field gradient $G\hat{r}$ applied along the direction \hat{r} for spatial encoding. In a frame rotating at the resonance frequency γB_0 , the precession frequency $\omega(t) = \gamma Gr(t)$ fluctuates reflecting the random motion of the molecular diffusion process [14, 15]. Here, $r(t)$ is the instantaneous position of the nuclear spin along the gradient direction and γ is the gyromagnetic ratio of the nucleus. The effective gradient strength may vary along time as $G(t)$, either by applying π -pulses if the gradient is constant or directly by modulating the gradient's sign and amplitude. The spins dephasing induced by the diffusion process is refocused by these control modulations forming the so-called spin-echoes [19, 20] (Fig. 1a,b). At the evolution time T_E of the control sequence, the spin-echo magnetization decays depending on how nuclear spins were scrambled by the diffusion process. The resulting magnetization at T_E is then spatially encoded with an MRI acquisition sequence.

The spins acquire a random phase $\phi(T_E)$ that typically follows a Gaussian distribution [28]. The magnetization in a voxel of the image becomes

$$M(T_E) = e^{-\frac{1}{2}\langle\phi^2(T_E)\rangle} M(0). \quad (1)$$

The quadratic phase is averaged over the spin ensemble as [14–16]

$$\langle\phi^2(T_E)\rangle = \gamma^2 \int_0^{T_E} dt \int_0^{T_E} dt' G(t)G(t') \langle\Delta r(t-t')\Delta r(0)\rangle, \quad (2)$$

which is expressed in terms of the control applied to the system by $G(t)$ and the molecular displacement autocorrelation function $\langle\Delta r(0)\Delta r(t)\rangle = D_0\tau_c e^{-|t|/\tau_c}$ [16–18]. Here $\Delta r(t) = r(t) - \langle r(t) \rangle$ is the instantaneous displacement of the spin position from its mean value, D_0 is the free diffusion coefficient, and τ_c is the correlation time of the diffusion process. The restriction length l_c of the microstructure compartment in which molecular diffusion is taking place is then determined by the Einstein-Diffusion equation $l_c^2 = D_0\tau_c$ [15]. Then, by *monitoring the spin-echo decay by applying suitable control sequences, one can infer microstructure-sizes* [17, 18, 21–23, 27].

Spin-echo decay-shift as a probing-microstructure paradigm. The spin-echo magnetization decay is usually characterized by its decay-rate [14, 15]. Under the control sequences discussed in Fig. 1a,b, the decay-rate is typically reduced as the number of refocusing periods N increases [20]. This effect is shown in Fig. 1a-c, where the Hahn spin-echo ($N=1$) decay is compared with the signal after a CPMG sequence ($N>1$) with multiple echoes [20]. However, in the *restricted diffusion* regime when the refocusing periods are longer than the correlation time τ_c , the spin-echo decays as $M(T_E)/M(0) \approx e^{-\gamma^2 G^2 D_0 \tau_c^2 (T_E - (1+2N)\tau_c)}$ (see Methods). There, the spins have been fully scrambled within the compartment, and the dephasing cannot be refocused leading to a decay-rate $\gamma^2 G^2 D_0 \tau_c^2$ independent of N . Yet, the spin-echo retains information of the transition

from the free to the restricted diffusion regime. This information is manifested as a “decay-shift” $\gamma^2 G^2 D_0 \tau_c^3 (1+2N)$ *independent of the evolution time* on the spin-echo decay signal, as shown in Fig. 1c. We here demonstrate that this shift can be exploited to selectively probe microstructure sizes as it is $\propto l_c^6$.

As this decay-shift depends on N , it can be selectively probed by concatenating a Hahn with a CPMG gradient modulation and changing the ratio between the relative refocusing periods of each component of the sequence as shown in Fig. 1d. This control sequence produces an effective modulated gradient $G(t)$, that conforms the Non-uniform Oscillating-Gradient Spin-Echo (NOGSE) [17, 18]. This sequence also factorizes out other relaxation mechanisms allowing to probe selectively the diffusion induced decay.

We define the NOGSE contrast (NOGSEc) as the amplitude ΔM given by the difference between the CPMG and the Hahn signal (Fig. 1c). It is obtained by evaluating NOGSE at the refocusing periods $t_C = t_H$ and then at $t_C \rightarrow 0$ using the definitions shown in Fig. 1d. Then both measurements are subtracted (see Methods). Within the restricted diffusion regime, this contrast amplitude is

$$\Delta M \approx e^{-\gamma^2 G^2 D_0 \tau_c^3 (\frac{T_E}{\tau_c} - 3)} \left(e^{\gamma^2 G^2 D_0 \tau_c^3 2(N-1)} - 1 \right), \quad (3)$$

which is very sensitive to the restricted diffusion length l_c as it has a parametric dependence $l_c^6 \propto \tau_c^3$ provided by the spin-echo decay-shift [17, 18].

NOGSE as a selective microstructure-size filter. NOGSEc ΔM has a *maximum* as a function of the normalized echo-time T_E/τ_c as shown in Fig. 1e. We exploit this maximum contrast to enhance the relative contribution to the signal from specific restriction lengths l_c from a size-distribution.

In order to perform a general analysis, Eq. (3) can be expressed in terms of dimensionless lengths $L_D = l_D/l_G$, $L_c = l_c/l_G$ (see Methods). Here, $l_c = \sqrt{D_0\tau_c}$, $l_D = \sqrt{D_0 T_E}$, $l_G = \sqrt[3]{D_0/\gamma G}$ are the restriction length, the diffusion length that the spin can diffuse freely during T_E and the dephasing diffusion length that provides a phase shift of 2π , respectively [15] (Fig. 1c). Then, ΔM as a function of L_c can be approximated by a Gaussian function when $L_D/L_c \gg 1$, $L_c^6 \ll 1$ and $L_D \gg 1$ (see Methods),

$$\Delta M \approx 2(N-1)e^{-3/2} (L_c^f)^6 \exp \left[-12 \left(\frac{L_c - L_c^f}{L_c^f} \right)^2 \right]. \quad (4)$$

NOGSEc therefore acts as a microstructure-size “bandpass-filter” with L_c^f as the filter-center size (see Fig. 2a)

$$L_c^f \approx (3/2)^{\frac{1}{4}} L_D^{-\frac{1}{2}}. \quad (5)$$

The filter-band selectivity is defined by the ratio between the full-width-at-half-maximum (FWHM) and L_c^f , $FWHM/L_c^f \approx \sqrt{\frac{\ln 2}{3}} \approx 0.5$.

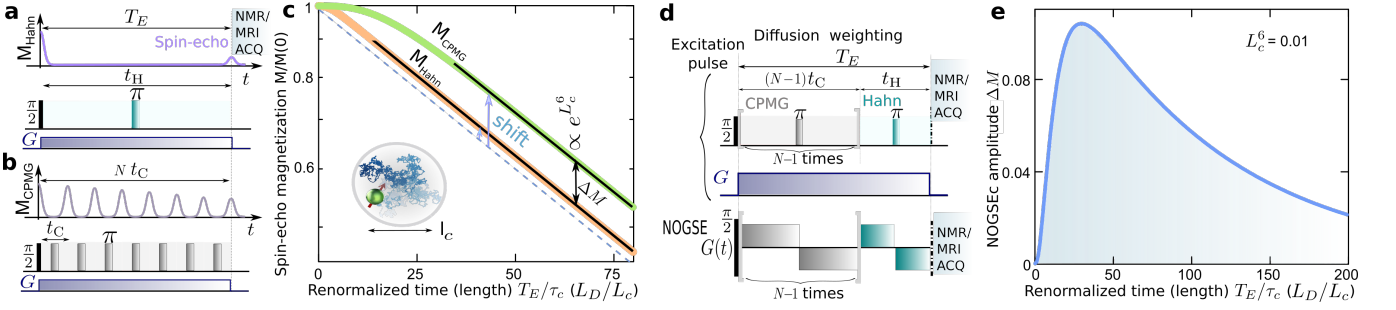


Figure 1. Spin-echo decay-shift as a paradigm for probing microstructure sizes. (a,b) Magnetic resonance spin-echo sequences for DWI. An initial $\frac{\pi}{2}$ -excitation pulse is followed by a constant magnetic field gradient G . During the evolution time T_E , equidistant π rf-pulses modulate the effective gradient $G(t)$, switching its sign for refocusing the spins dephasing induced by the diffusion process to form the spin-echoes. (a) Hahn sequence with a refocusing period t_H ($N=1$). (b) CPMG sequence with $N > 1$ refocusing periods of duration t_C . After T_E the remaining signal is measured, possibly using MRI acquisition encoding. (c) Spin-echo decay for the Hahn ($N=1$, orange line) and the CPMG ($N=8$, green line) gradient modulation as a function of the normalized evolution time T_E/τ_c , where τ_c is the correlation time of the restricted diffusion process. For both sequences, when the refocusing period is $T_E/N \gg \tau_c$, the decaying signal $\propto \exp(-\gamma^2 G^2 D_0 \tau_c^2 T_E)$ (black solid-lines) has a constant decay-rate independent of N . However, the curves have a decay-shift $\propto \exp(\gamma^2 G^2 D_0 \tau_c^3 (1+2N))$ independent of time but depending on N (marked with arrows) with respect to the dashed-line that gives $\exp(-\gamma^2 G^2 D_0 \tau_c^2 T_E)$. The contrast ΔM between the CPMG and Hahn decay is highlighted in the plot with double-arrow. The inset shows a scheme for molecules undergoing restricted Brownian motion. The diffusion restriction length $l_c = \sqrt{D_0 \tau_c}$ is related to the compartment-size. (d) A CPMG sequence of $N-1$ equidistant refocusing periods t_C is concatenated with a Hahn sequence of refocusing period t_H [17]. The effective modulated gradient $G(t)$ is shown at the bottom, and it composes the Non-uniform Oscillating-Gradient Spin-Echo (NOGSE) sequence that can be generated by directly modulating the gradient strength [18]. (e) NOGSE contrast (NOGSEc) ΔM as a function of the normalized evolution time $\frac{T_E}{\tau_c}$ for $L_c^6 = \gamma^2 G^2 D_0 \tau_c^3 = 0.01$. This value is representative of white-matter tissue considering $D_0 = 0.7 \mu\text{m}^2/\text{ms}$ and $\tau_c = 1.5 \text{ ms}$ with $G = 240 \text{ mT/m}$ and $N = 8$.

The maximum of ΔM at the size L_c^f can be tuned to highlight a given restriction length l_c based on choosing properly the sequence control parameters, i.e. the gradient strength G and the evolution time T_E (see Fig. 2a).

The filtered size decreases with increasing the control parameter L_D according to Eq. (5). At the same time, increasing L_D decreases the contrast amplitude which is $\propto (L_c^f)^6 \propto 1/L_D^3$. Therefore, the minimum size that can be filtered in practice is limited by the Signal-to-Noise Ratio (SNR) and the maximum achievable gradient strength as $L_D \propto \sqrt[3]{G}$. This decrease of ΔM can be compensated linearly with increasing the number of refocusing periods N , as long as $\frac{L_D^2}{L_c^2 N} = \frac{T_E}{\tau_c N} \gg 1$ to reach the restricted regime (see Eq. (4) and Fig. 2b).

A practical limitation is also the unavoidable transversal T_2 -relaxation due to the intrinsic dephasing of the nuclear spins. NOGSEc decays then as

$$\Delta M_{T_2} = \Delta M e^{-L_2^2/L_D^2}, \quad (6)$$

where we have defined $L_2 = \frac{l_2}{l_G}$ as the T_2 diffusion dimensionless length with $l_2 = (D_0 T_2)^{1/2}$. The T_2 -relaxation effect is showed in Fig. 2c for different values of L_2^2 . Remarkably, the filter shape and center remains the same as the case of $T_2 \rightarrow \infty$.

Selective size-filtering in typical microstructure-size distributions. Our results show that one can produce quantitative images based on a signal contrast generated by specific microstructure-sizes from a size-distribution. This

method avoids extracting the microstructure-size by fitting a curve, which is time consuming as it typically requires several measurements [11, 23–27]. The filter amplitude ΔM in Eq. (4) remains constant by varying the gradient strength and the evolution time keeping fixed the parameter L_D , as shown in Fig. 2d-e. We exploit this property for a proof-of-principle evaluation of the performance of the NOGSEc filter applied to microstructural size-distribution inherent to heterogeneous biological tissues as shown in Fig. 3. Typical size-distributions $P(l_c)$ are log-normal and bi-modal functions [7, 24, 26, 29, 30] as shown in Figs. 3a-b. NOGSEc for a size-distribution is given by

$$\Delta M = \int_{l_c} P(l_c) \Delta M(l_c) dl_c, \quad (7)$$

where $\Delta M(l_c)$ is the contribution for a given restriction length l_c . Figures 3c-d show ΔM as a function of $l_c^f = L_c^f l_G$, where G and T_E are changed simultaneously keeping L_D^2 constant. The center of the filter at l_c^f is therefore swept while the filter amplitude is kept constant. The resulting filtered signal as a function of the filter center l_c^f therefore resembles the original size-distributions, where the log-normal peak and both Gaussian peaks are clearly identified. The effects of T_2 -relaxation are shown in Fig. 3c for typical values of white-matter tissue. To further demonstrate the filter selectivity, Figure 3d shows that if one chooses l_c^f equal to the center of one of the two Gaussian distributions, the other component is filtered-out. These simulations demonstrate

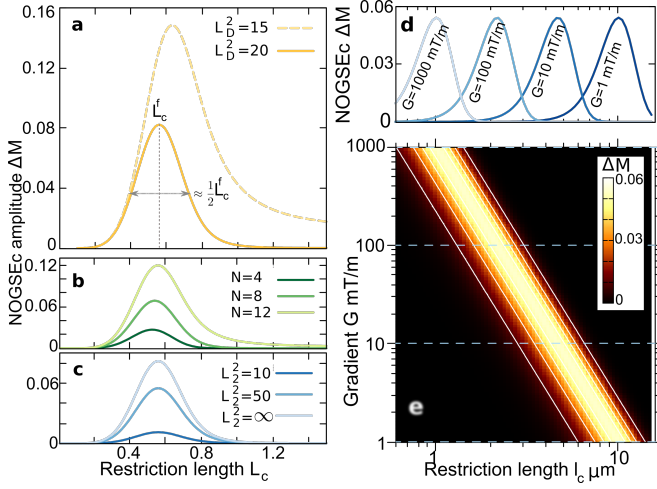


Figure 2. Selective microstructure-size filter based on NOGSE contrast. (a) NOGSEc amplitude ΔM as a function of the renormalized restriction length L_c for different values of the diffusion length L_D ($L_D^2 = 15, 20$ with $N=8$ refocusing periods). ΔM shows a Gaussian filter functional dependence for $L_D \gg 1$ with a maximum at $L_c^f \propto L_D^{-\frac{1}{2}}$. The filter full-width-half-maximum $FWHM \approx \frac{L_c^f}{2}$. (b) The amplitude of ΔM at L_c^f increases linearly with the refocusing periods N as long as $\frac{L_D^2}{L_c^2 N} \gg 1$. Here $L_D^2 = 22$. (c) Attenuation effects of the filter amplitude due to transversal T_2 -relaxation. Different dephasing diffusion lengths $L_2^2 = 10, 50, \infty$ associated to T_2 are shown for $L_D^2 = 20$. ΔM decreases with decreasing L_2 . (d,e) ΔM as a function of the restriction length l_c and the gradient strength G , considering $N=8$. As $L_D^2 = 25$ remains constant by properly varying T_E , the maximum ΔM is also constant. The considered dynamic range for the gradient strength G is achievable with current technologies. The horizontal dashed lines in (e) correspond to the specific cases plotted in (d). L_c^f increases with decreasing G . $D_0 = 0.7 \mu\text{m}^2/\text{ms}$ is considered.

the feasibility of performing *quantitative images of a selective microstructure-size l_c^f based on the NOGSEc amplitude as a “bandpass” filter.*

The transversal T_2 -relaxation limits the largest microstructure-size that can be filtered, as the restricted diffusion regime has to be achieved. A good SNR for ΔM is only obtained for $L_c < L_D < L_2$. For short T_2 , the strategy is therefore using the lowest possible value of L_D and reducing the number of refocusing periods N so as to remain in the restricted regime. We consider this scenario in proof-of-principle experiments and perform a size-filter sweep varying only the gradient amplitude while keeping $T_E \lesssim T_2$ constant. We implement the microstructure-size filter method on an ex-vivo mouse brain focusing on the Corpus Callosum (CC) region (see experimental details in Methods). The CC contains aligned axons and is a paradigmatic model for log-normal size-distributions [7, 24, 26, 29, 30]. Figure 4a shows images of ΔM for two gradient strengths. The largest gradient acts as a “bandpass” Gaussian-filter of the lower microscopic sizes

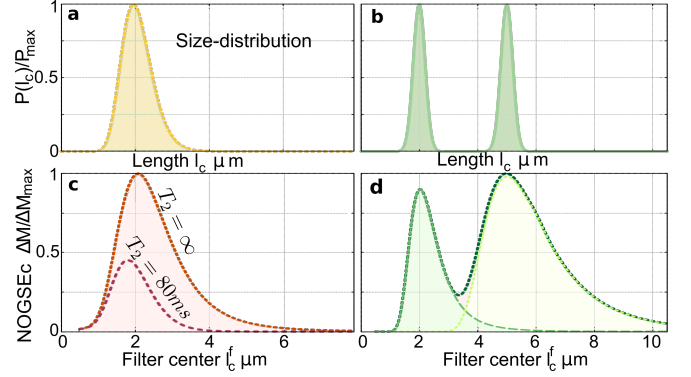


Figure 3. Selective size-filtering with NOGSE contrast in typical microstructure size-distributions. Size-distribution probability $P(l_c)$ for two typical cases of tissue microstructure, (a) a log-normal distribution with median $2 \mu\text{m}$ and geometric standard deviation $1.22 \mu\text{m}$, representative of white matter size-distributions; and (b) a bimodal Gaussian distribution with means $l_c = 2 \mu\text{m}$ and $l_c = 5 \mu\text{m}$, and a standard deviation $0.2 \mu\text{m}$ for both peaks. (c,d) Normalized NOGSEc amplitude ΔM as a function of the filter center l_c^f . The diffusion coefficient is $D_0 = 0.7 \mu\text{m}^2/\text{ms}$ in both cases. (c) ΔM including transversal T_2 -relaxation effects (dashed line, $T_2 = 80 \text{ ms}$) is contrasted with the ideal case without relaxation effects (solid line, $T_2 = \infty$) for the distribution of panel (a). Here $L_D^2 = 11$, $N = 4$ and $\Delta M_{\text{max}} = 0.08$. (d) The dashed lines show ΔM obtained considering separately each of the component of the bimodal distribution of panel (b). The low overlap between the dashed lines demonstrates the filtering property of NOGSEc. Here $L_D^2 = 25$, $N = 8$ and $\Delta M_{\text{max}} = 0.027$.

of the distribution, compared to the weaker gradient that acts as a “high-pass” filter of the larger sizes (Fig. 4b). Therefore Fig. 4a clearly highlights zones of the CC with complementary colors depending of the microstructure-size. This is demonstrated quantitatively in Fig. 4b-c for three regions-of-interest (ROI). The average ΔM as a function of the gradient for the ROIs is shown in Fig. 4c together with fitted curves derived from our theoretical model following Eq. (7) (see Methods). The inferred microstructure-size distributions and the ΔM filter shapes are shown in Fig. 4b. The excellent agreement between the model and the experimental data fully demonstrates the reliability of the quantitative images shown in panel a based on the NOGSE microstructure-size filter and the assumed log-normal model.

Conclusions. The presented results introduce a method for performing non-invasive quantitative images of selective microstructure-sizes based on probing nuclear-spin dephasing induced by molecular diffusion with magnetic resonance. Conversely to standard diffusion-weighted imaging approaches that are based on observing the decay-rate of the spin signal, we exploit dynamical control with oscillating gradients to selectively probe a decay-shift on spin-echo decays. This decay-shift contains quantitative information of microstructure-sizes that restrict the molecular

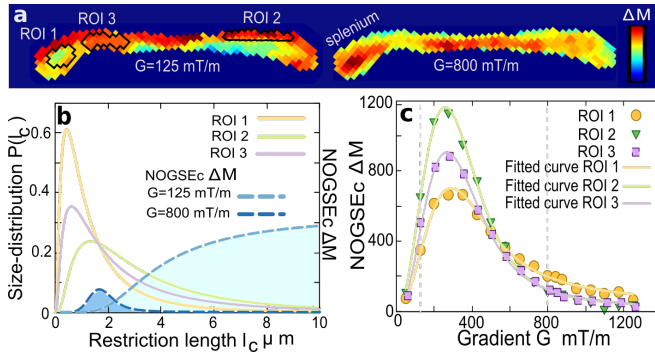


Figure 4. Non-invasive NOGSE-imaging of selective microstructure-sizes in ex-vivo mouse brain. (a) Two images based on NOGSEc of the Corpus Callosum region of a mouse brain for two gradient strengths. The ΔM contrast highlights different zones with complementary colors when comparing the images for the two gradients. The color scale covers the full range of contrast signal in each image. Three regions-of-interest (ROI) are indicated in black contours. The images were acquired for $N=2$ and $T_E=21.5$ ms. Pixel-size $78 \times 78 \mu\text{m}^2$. (see more details in Methods). (b) Size-distributions (solid-lines) that best fit the experimental data for the selected ROIs. The dashed lines show $\Delta M(l_c)$ predicted by our model for the two gradients used in (a). The predicted overlap between the reconstructed distribution and the $\Delta M(l_c)$ filter is consistent with the signal contrast shown in (a and c): ROI 1 has lower sizes than ROI 2 and 3, and therefore ROI 1 has higher ΔM for $G = 800$ mT/m; conversely ROI 2 and 3 have higher contrast amplitude for $G = 125$ mT/m. (c) Average NOGSEc signal (symbols) as a function of the gradient strength G for the three ROIs. The vertical dashed lines mark the gradient strengths used in (a). The solid lines are fits to the experimental data of our theoretical model following Eq. (7) for a log-normal distribution. The fitted parameters are the median 1.08 ± 0.06 , 2.82 ± 0.01 and $1.87 \pm 0.04 \mu\text{m}$ and the geometric standard deviation 2.58 ± 0.03 , 2.39 ± 0.02 and $2.91 \pm 0.04 \mu\text{m}$ for ROI 1, 2 and 3, respectively. We considered a uniform $D_0 = 0.7 \mu\text{m}^2/\text{ms}$ as a representative diffusion coefficient to fit the size-distribution.

diffusion. We generate a contrast amplitude that behaves as a microstructure-size filter to selectively probe a restriction length determined by the control parameters. We show the usefulness and performance of the method with proof-of-principle simulations and experiments on typical size-distributions of white-matter tracts in a mouse brain. A quantitative image of specific diffusion restriction lengths is performed extracted from only two images, allowing to significantly reduce the tens of images that typically demand the inference of microstructure-sizes from data fittings [11, 23–27]. Even though intrinsic T_2 -relaxation may represent a limitation, we show excellent performance probing quantitative information of microstructure details between $\sim 0.1 - 10 \mu\text{m}$ on biological tissue as in the mouse white matter, being able to filter sizes much lower than the present image resolution. This work lays the foundations of a novel conceptual tool with low overhead for designing

quantitative methods for non-invasive imaging of tissue microstructure. This diagnostic tool opens up a new avenue to explore for in-vivo imaging. In addition, these results can also be applied for characterizing material microstructures, such as rocks which are of particular interest for oil extraction, and for nanoscale-imaging of biological tissues with novel quantum sensors based on noise spectroscopy [1–3].

Acknowledgments. We acknowledge Soledad Espósito and Micaela Kortsarz for preparing the ex-vivo mouse brain, and Federico Turco for scripting assistance to process the experimental data. We thank Lucio Frydman and Jorge Jovicich for fruitful discussions. This work was supported by CNEA, ANPCyT-FONCyT PICT-2017-3447, PICT-2017-3699, PICT-2018-04333, PIP-CONICET (11220170100486CO), UNCuyo SHIP Tipo I 2019-C028, Instituto Balseiro. A.Z. and G.A.A. are members of the Research Career of CONICET. M.C. and P.J. acknowledge support from the Instituto Balseiro’s fellowships.

* analina.zwick@cab.cnea.gov.ar

† gonzalo.alvarez@cab.cnea.gov.ar

- [1] T. Staudacher, N. Raatz, S. Pezzagna, J. Meijer, F. Reinhard, C. A. Meriles, and J. Wrachtrup, *Nat. Commun.* **6**, 8527 (2015).
- [2] P. Wang, S. Chen, M. Guo, S. Peng, M. Wang, M. Chen, W. Ma, R. Zhang, J. Su, X. Rong, F. Shi, T. Xu, and J. Du, *Sci. Adv.* **5**, eaau8038 (2019), <https://advances.sciencemag.org/content/5/4/eaau8038.full.pdf>.
- [3] J. F. Barry, M. J. Turner, J. M. Schloss, D. R. Glenn, Y. Song, M. D. Lukin, H. Park, and R. L. Walsworth, *Proc. Natl. Acad. Sci. U.S.A.* **113**, 14133 (2016), <https://www.pnas.org/content/113/49/14133.full.pdf>.
- [4] D. R. Glenn, K. Lee, H. Park, R. Weissleder, A. Yacoby, M. D. Lukin, H. Lee, R. L. Walsworth, and C. B. Connolly, *Nat. Methods* **12**, 736 (2015).
- [5] A. R. Padhani, G. Liu, D. M. Koh, T. L. Chenevert, H. C. Thoeny, T. Takahara, A. Dzik-Jurasz, B. D. Ross, M. Van Cauteren, D. Collins, D. A. Hammoud, G. J. S. Rustin, B. Taouli, and P. L. Choyke, *Neoplasia* **11**, 102 (2009).
- [6] V. Drago, C. Babiloni, D. Bartrés-Faz, A. Caroli, B. Bosch, T. Hensch, M. Didic, H.-W. Klafki, M. Pievani, J. Jovicich, L. Venturi, P. Spitzer, F. Vecchio, P. Schoenknecht, J. Wiltfang, A. Redolfi, G. Forloni, O. Blin, E. Irving, C. Davis, H.-g. Hårdemark, and G. B. Frisoni, *J. Alzheimers Dis.* **26**, 159 (2011).
- [7] N. S. White, T. B. Leergaard, H. D’Arceuil, J. G. Bjaalie, and A. M. Dale, *Hum. Brain Mapp.* **34**, 327 (2013).
- [8] N. S. White, C. R. McDonald, N. Farid, J. Kuperman, D. Karow, N. M. Schenker-Ahmed, H. Bartsch, R. Rakow-Penner, D. Holland, A. Shabai, A. Bjørnerud, T. Hope, J. Hattangadi-Gluth, M. Liss, J. K. Parsons, C. C. Chen, S. Raman, D. Margolis, R. E. Reiter, L. Marks, S. Kesari, A. J. Mundt, C. J. Kaine, B. S. Carter, W. G. Bradley, and A. M. Dale, *Cancer Res.* **74**, 4638 (2014).
- [9] C. Enzinger, F. Barkhof, O. Ciccarelli, M. Filippi, L. Kappos, M. A. Rocca, S. Ropele, Å. Rovira, T. Schneider, N. de Stefano, H. Vrenken, C. Wheeler-Kingshott, J. Wuer-

- fel, F. Fazekas, and o. and, *Nat. Rev. Neurol.* **11**, 676 (2015).
- [10] D. Le Bihan, *Nat. Rev. Neurosci.* **4**, 469 (2003).
 - [11] J. Xu, H. Li, K. D. Harkins, X. Jiang, J. Xie, H. Kang, M. D. Does, and J. C. Gore, *Neuroimage* **103**, 10 (2014).
 - [12] F. Grussu, T. Schneider, C. Tur, R. L. Yates, M. Tachrount, A. Ianuş, M. C. Yiannakas, J. Newcombe, H. Zhang, D. C. Alexander, G. C. DeLuca, and C. A. M. Gandini Wheeler-Kingshott, *Ann. Clin. Transl. Neurol.* **4**, 663 (2017).
 - [13] D. C. Alexander, T. B. Dyrby, M. Nilsson, and H. Zhang, *NMR Biomed.* **32**, e3841 (2019), eprint: <https://onlinelibrary.wiley.com/doi/pdf/10.1002/nbm.3841>.
 - [14] D. S. Grebenkov, *Rev. Mod. Phys.* **79**, 1077 (2007).
 - [15] P. T. Callaghan, *Translational Dynamics and Magnetic Resonance: Principles of Pulsed Gradient Spin Echo NMR* (Oxford University Press, Oxford, 2011).
 - [16] J. Stepisnik, *Physica B* **183**, 343 (1993).
 - [17] G. A. Álvarez, N. Shemesh, and L. Frydman, *Phys. Rev. Lett.* **111**, 080404 (2013).
 - [18] N. Shemesh, G. A. Álvarez, and L. Frydman, *J. Magn. Reson.* **237**, 49 (2013).
 - [19] E. Hahn, *Phys. Rev.* **80**, 580 (1950).
 - [20] H. Y. Carr and E. M. Purcell, *Phys. Rev.* **94**, 630 (1954).
 - [21] I. Drobnjak, H. Zhang, A. Ianus, E. Kaden, and D. C. Alexander, *Magn. Reson. Med.* **75**, 688 (2016), <https://onlinelibrary.wiley.com/doi/pdf/10.1002/mrm.25631>.
 - [22] M. Nilsson, S. Lasic, I. Drobnjak, D. Topgaard, and C.-F. Westin, *NMR Biomed.* **30**, e3711 (2017), e3711 nbm.3711, <https://onlinelibrary.wiley.com/doi/pdf/10.1002/nbm.3711>.
 - [23] D. S. Novikov, E. Fieremans, S. N. Jespersen, and V. G. Kiselev, *NMR Biomed.* **32**, e3998 (2019).
 - [24] Y. Assaf, T. Blumenfeld-Katzir, Y. Yovel, and P. J. Basser, *Magn. Reson. Med.* **59**, 1347 (2008), <https://onlinelibrary.wiley.com/doi/pdf/10.1002/mrm.21577>.
 - [25] D. C. Alexander, P. L. Hubbard, M. G. Hall, E. A. Moore, M. Ptito, G. J. Parker, and T. B. Dyrby, *Neuroimage* **52**, 1374 (2010).
 - [26] N. Shemesh, G. A. Álvarez, and L. Frydman, *PLoS One* **10**, e0133201 (2015).
 - [27] H. H. Ong and F. W. Wehrli, *Neuroimage* **51**, 1360 (2010).
 - [28] J. Stepisnik, *Physica B* **270**, 110 (1999).
 - [29] S. Pajevic and P. J. Basser, *PLoS One* **8**, e54095 (2013).
 - [30] D. Liewald, R. Miller, N. Logothetis, H.-J. Wagner, and A. Schüz, *Biol. Cybern.* **108**, 541 (2014).

METHODS

Magnetization decay of an spin ensemble under dynamical control. The magnetization signal observed from an ensemble of non-interacting and equivalent spins, under the effect of dynamical control, is $M(t) = \langle e^{-i\phi(t)} \rangle M(0)$. Here, the brackets denote the ensemble average over the random phases $\phi(t)$ acquired by the spins during the evolution time t . For the considered dynamical control with modulated gradient spin-echo sequences, the average phase becomes null, $\langle \phi(t) \rangle = 0$. Then, as $\phi(t)$ typically follows

a Gaussian distribution [28], the signal will depend on the random phase variance $M(t) = e^{-\frac{1}{2}\langle \phi^2(t) \rangle} M(0)$.

The variance expressed in terms of the control applied to the system by $G(t)$ and the molecular displacement auto-correlation function $\langle \Delta r(0)\Delta r(t) \rangle = D_0\tau_c e^{-|t|/\tau_c}$ [16–18] is given in Eq. (2) of the main text.

For a piecewise constant modulation $G(t)$, that switches N times its sign at times t_i with $i = 0..N-1$ during the evolution time T_E . The quadratic phase of the magnetization decay is

$$\begin{aligned} \langle \phi^2(T_E) \rangle &= \gamma^2 G^2 D_0^2 \tau_c \sum_{i=0}^{N-1} \sum_{j=0}^{N-1} \int_{t_i}^{t_{i+1}} \int_{t_j}^{t_{j+1}} e^{-|t-t'|/\tau_c} (-1)^i (-1)^j dt' dt \\ &= \gamma^2 G^2 D_0^2 \tau_c \sum_{i=0}^{N-1} \sum_{j=0}^{N-1} (-1)^i (-1)^j \left[\left(\begin{cases} 2\tau_c t_j - \tau_c^2 e^{-\frac{t_i-t_j}{\tau_c}} & t_j \leq t_i \\ -\tau_c^2 e^{-\frac{t_i-t_j}{\tau_c}} & t_i < t_j \end{cases} \right) \right. \\ &\quad + \left(\begin{cases} 2\tau_c t_{j+1} - \tau_c^2 e^{-\frac{t_{i+1}-t_{j+1}}{\tau_c}} & t_{j+1} \leq t_{i+1} \\ -\tau_c^2 e^{-\frac{t_{i+1}-t_{j+1}}{\tau_c}} + 2\tau_c t_{i+1} & t_{i+1} < t_{j+1} \end{cases} \right) - \left(\begin{cases} 2\tau_c t_j - \tau_c^2 e^{-\frac{t_{i+1}-t_j}{\tau_c}} & t_j \leq t_{i+1} \\ -\tau_c^2 e^{-\frac{t_{i+1}-t_j}{\tau_c}} + 2\tau_c t_{i+1} & t_{i+1} < t_j \end{cases} \right) \\ &\quad \left. - \left(\begin{cases} 2\tau_c t_{j+1} - \tau_c^2 e^{-\frac{t_i-t_{j+1}}{\tau_c}} & t_{j+1} \leq t_i \\ -\tau_c^2 e^{-\frac{t_i-t_{j+1}}{\tau_c}} + 2\tau_c t_i & t_i < t_{j+1} \end{cases} \right) \right]. \end{aligned} \quad (8)$$

Magnetization decay within the restricted diffusion regime. In the restricted diffusion regime all terms \propto

$e^{-\frac{|t_i-t_j|}{\tau_c}} \rightarrow 0$ as $|t_i-t_j| \gg \tau_c$ for all $i \neq j$, therefore the non-null terms in Eq. (8) are those with $i = j$. The phase variance is then

$$-\frac{1}{2} \langle \phi^2(T_E) \rangle = -\frac{1}{2} \gamma^2 G^2 D_0^2 \tau_c \sum_{i=0}^{N-1} \sum_{j=0}^{N-1} (-1)^i (-1)^j \left[\left(2\tau_c t_j - \tau_c^2 e^{-\frac{t_i-t_j}{\tau_c}} \right) \delta_{ij} + \left(2\tau_c t_{j+1} - \tau_c^2 e^{-\frac{t_{i+1}-t_{j+1}}{\tau_c}} \right) \delta_{i+1,j+1} \right. \quad (9)$$

$$\left. - \left(2\tau_c t_j - \tau_c^2 e^{-\frac{t_{i+1}-t_j}{\tau_c}} \right) \delta_{i+1,j} - \left(2\tau_c t_{j+1} - \tau_c^2 e^{-\frac{t_i-t_{j+1}}{\tau_c}} \right) \delta_{i,j+1} \right] \\ = -\frac{1}{2} \gamma^2 G^2 D_0^2 \tau_c \left[2\tau_c \sum_{i=1}^N (t_i - t_{i-1}) - \tau_c^2 (4N + 2) \right] \quad (10)$$

$$= -\gamma^2 G^2 D_0^2 \tau_c^2 [T_E - (2N + 1)\tau_c]. \quad (11)$$

Then, the *decay-rate* is $\frac{d\langle \phi^2(T_E) \rangle}{dT_E} = \gamma^2 G^2 D_0^2 \tau_c^2$, and the *decay-shift* is the time-independent term $\gamma^2 G^2 D_0^2 \tau_c^3 (2N + 1)$, which can also be derived from

$$\gamma^2 G^2 D_0 \tau_c^3 (2N + 1) = \gamma^2 G^2 D_0 \tau_c (2N + 1) \int_0^\infty dt t \langle \Delta r(0)\Delta r(t) \rangle. \quad (12)$$

NOGSE contrast amplitude. One can obtain an analytical expression for the magnetization decay in Eq. (8) for the Hahn, CPMG and NOGSE spin-echo sequences described in

Fig. (1) of the main text. In the restricted diffusion regime $T_E, t_H, t_C \gg \tau_c$, they result

$$\begin{aligned} M_{\text{Hahn}}(t_H) &= \exp\{-\gamma^2 G^2 D_0 \tau_c^3 [\frac{t_H}{\tau_c} - 3]\}, \\ M_{\text{CPMG}}(N t_C, N) &= \exp\{-\gamma^2 G^2 D_0 \tau_c^3 [\frac{N t_C}{\tau_c} - (2N + 1)]\}, \\ M_{\text{NOGSE}}(T_E, N, t_C) &= \exp\{-\gamma^2 G^2 D_0 \tau_c^3 [\frac{T_E}{\tau_c} - (2N + 1)]\}, \end{aligned} \quad (13)$$

with $T_E = (N - 1)t_C + t_H$.

We define the NOGSE contrast (NOGSEc) amplitude ΔM to the difference between $M_{\text{NOGSE}}(T_E, N, t_C = t_H) = M_{\text{CPMG}}(\frac{T_E}{N}, N)$ and $M_{\text{NOGSE}}(T_E, N, t_C \rightarrow 0) \simeq M_{\text{Hahn}}(T_E)$, i.e.

$$\Delta M(T_E, N) = M_{\text{CPMG}}(T_E, N) - M_{\text{Hahn}}(T_E). \quad (14)$$

Then, we arrive to Eq. (3) of the main text by introducing Eq. (13) into Eq. (14)

$$\Delta M \approx e^{-\gamma^2 G^2 D_0 \tau_c^3 (\frac{T_E}{\tau_c} - 3)} \left(e^{\gamma^2 G^2 D_0 \tau_c^3 2(N-1)} - 1 \right). \quad (15)$$

NOGSEc results

$$\Delta M(L_D, L_c, N) = e^{-L_c^4 (L_D^2 - 3L_c^2)} (e^{2(N-1)L_c^6} - 1), \quad (16)$$

within the restricted diffusion regime, using the dimensionless variables L_D, L_c defined in the main text.

The general expression for ΔM that includes all diffusion time scales can be obtained from Eq. (8) by replacing the time intervals as defined in Fig. 1c of the main text.

Gaussian microstructure-size filter derivation. The NOGSEc amplitude in the restricted diffusion regime, Eq. (16), can be approximated by

$$\Delta M \approx e^{-L_c^4 (L_D^2 - 3L_c^2)} 2(N-1)L_c^6, \quad (17)$$

for $L_c \ll 1$. The maximum of ΔM occurs at $\frac{d\Delta M}{dL_c} = 0$. In the asymptotic limit of $L_D \gg 1$, it is achieved for

$$L_c = L_c^f \approx (3/2)^{\frac{1}{4}} L_D^{-\frac{1}{2}} + \mathcal{O}(L_D^{-\frac{7}{2}}), \quad (18)$$

where L_c^f is the center of the filter as described in Eq. (5) of the main text.

The NOGSEc amplitude can be approximated by

$$\begin{aligned} \Delta M &\approx e^{-3/2} 3\sqrt{\frac{3}{2}} (N-1) L_D^{-3} \\ &\quad - 36e^{-3/2} (N-1) L_D^{-2} (L_c - L_c^f)^2 + \mathcal{O}((L_c - L_c^f)^4), \end{aligned} \quad (19)$$

with a Taylor expansion in L_c at $L_c \approx L_c^f$ of the expression given in Eq. (17). We use this expansion to define the first

moments of the Gaussian filter function of Eq. (4) in the main text, obtaining

$$\Delta M \approx 2(N-1)e^{-3/2} (L_c^f)^6 \exp \left[-12 \left(\frac{L_c - L_c^f}{L_c^f} \right)^2 \right]. \quad (20)$$

This expression is then verified to approximate very well the exact expression derived from Eq. (8) within the regime of $L_D \gg 1$ and $L_c \ll 1$.

Ex-vivo mouse brain preparation. The experiments were approved by the Institutional Animal Care and Use Committee of the Comisión Nacional de Energía Atómica under protocol number 08_2018. One mouse was sacrificed by isoflurane overdose and its brain was fixed in formaline. The brain was washed twice with PBS prior to the insertion into a 15 ml falcon tube filled with PBS. The brain was left in the magnet for at least three hours prior to the reported experiments to reach thermal equilibration.

MRI experiments. The experiments were performed on a 9.4T Bruker Avance III HD WB NMR spectrometer with a ¹H resonance frequency of $\omega_z = 400.15$ MHz. We use a Micro 2.5 probe capable of producing gradients up to 1500 mT/m in three spatial directions. The experiments temperature was stabilized at 21°C. We programmed and implemented with Paravision 6 the NOGSE MRI sequence shown in Fig. 5. The sequence parameters were: Repetition time 2000 ms, $T_{\text{echo time}} = 55\text{ms}$, FOV = 15x15 mm² with a matrix size of 192x192, leading to an in-plane resolution of $78 \times 78 \mu\text{m}^2$, and slice thickness of 1 mm with 128 signal averages. The two images were acquired with echo planar imaging (EPI) encoding with 4 segments (image acquisition time ≈ 17 min) and then subtracted to generate ΔM . The NOGSE modulation time was $T_E = 21.5\text{ms}$ with $N = 2$. The NOGSE gradients were applied perpendicular to the main axis of the axons in the corpus callosum. NOGSEc ΔM is determined from an image generated with $t_H = t_C = 10.75\text{ms}$ for the CPMG modulation and with $t_H = 0.5\text{ms}$ and $t_C = 21\text{ms}$ for the Hahn modulation. The set of parameter values were chosen for achieving good SNR for performing the proof-of-principle experiments. Further studies should be considered to explore the optimal values for acquiring the images in the shortest possible time.

Experimental data analysis. The mean signal from the pixels in the ROIs of Fig. 4a of the main text was analyzed, and plotted as a function of G in Fig. 4c. Fittings to the theoretical model were done assuming a uniform $D_0 = 0.7 \mu\text{m}^2/\text{ms}$ and a log-normal distribution $P(l_c) = \frac{1}{\sqrt{2\pi}\sigma l_c} e^{-\frac{(\ln(l_c) - \mu)^2}{2\sigma^2}}$ with median e^μ and geometric standard deviation e^σ . This implies that no extra assumptions were considered for the tissue model (e.g., intra/extracellular compartments). Therefore a single log-normal distribution was thus fitted to the experimental data, regardless of the potential heterogeneity. This means that all underlying compartments (e.g., extracellular, intracellular, etc.)

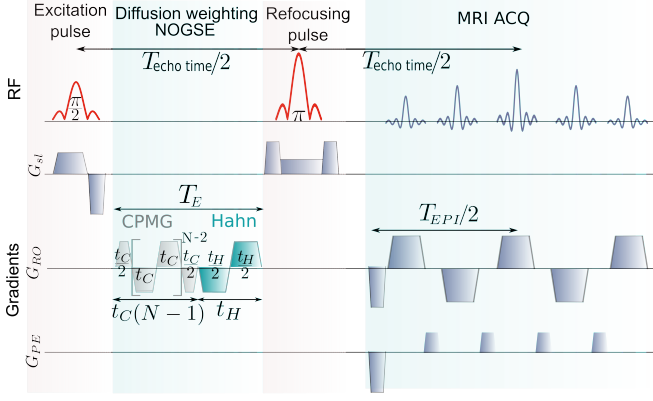


Figure 5. **Scheme for the experimental implementation of the NOGSE sequence.** An initial selective RF-excitation $\frac{\pi}{2}$ -pulse is applied to select a tissue slice. It is followed by a NOGSE gradient modulation of duration T_E following the scheme described in Fig. 1d of the main text. During the evolution time T_E , the gradient strength and sign is modulated with trapezoidal shapes. Then a selective RF π -pulse is applied to refocus magnetic field inhomogeneities. At the end a spatial EPI-encoding is applied for acquiring an image. Three gradients are applied in the three spatial directions for slide selection G_{sl} , for read orientation G_{RO} and phase encoding G_{PE} . The NOGSE gradients can be applied in arbitrary orientations.

reflected in the diffusion weighted are assumed to be described by a single log-normal distribution. We considered a distribution of restriction lengths l_c without assuming particular geometries. Remarkably the excellent agreement of the fitted curves to the experimental data in Fig. 4c is consistent with these simple assumptions.